Quantitative electron energy-loss spectroscopy (EELS) analyses of lead zirconate titanate

P. Harkins[a], M. MacKenzie[a*], A.J. Craven[a] and D.W. McComb[b]

[a]Department of Physics & Astronomy, University of Glasgow, Glasgow, G12 8QQ, UK

[b]Department of Materials and London Centre for Nanotechnology, Imperial College London, London, SW7 2AZ, UK

ABSTRACT

Electron energy-loss spectroscopy (EELS) analyses have been performed on a sol-gel deposited lead zirconate titanate film, showing that EELS can be used for heavy as well as light element analysis. The elemental distributions within the sol-gel layers are profiled using the Pb $N_{6,7}$- edges, Zr M-edges, Ti L-edges and O K-edge. A multiple linear least squares fitting procedure was used to extract the Zr signal which overlaps with the Pb signal. Excellent qualitative information has been obtained on the distribution of the four elements. The non-uniform and complementary distributions of Ti and Zr within each sol-gel deposited layer are observed. The metal:oxygen elemental ratios are quantified using experimental standards of $PbTiO_3$, $PbZrO_3$, ZrO_2 and TiO_2 to provide relevant cross-section ratios. The quantitative results obtained for Ti/O and Pb/O are very good but the Zr/O results are less accurate. Methods of further improving the results are discussed.

Keywords: EELS; PZT; MLLS; Heavy metal; quantification

*Corresponding author: m.mackenzie@physics.gla.ac.uk; tel. +44 (0)141 330 5580; fax. +44 (0)141 330 4464

1. Introduction

Electron energy-loss spectroscopy (EELS) and energy dispersive X-ray spectroscopy (EDX) are widely used as complementary analytical techniques in the analytical transmission electron microscope (TEM). However, while they can be performed simultaneously, the EELS acquisition conditions in the TEM are not optimised for EDX, with the result that there is a detrimental effect on the quality of EDX data obtained because of the relatively short counting times typically used for EELS. Traditionally EELS has been preferred for analysing light elements and EDX for analysing heavy elements, although there is a lot of overlap in practice. Many materials systems of current interest contain a mixture of light and heavy elements and it would be advantageous if a single analytical technique could be used for analyses of all the elements present in the system. Ultrathin window or windowless X-ray detectors can detect light elements but quantification is difficult because of severe self-absorption of low energy X-rays and their poor detection efficiency combined with the low fluorescence yield.

Hofer and Kothleitner (1996) have previously successfully applied EELS to study compositions of materials containing La and/or Ba. Here we report on our investigations of the ability of EELS to analyse heavy elements in a lead zirconate titanate (PZT) thin film. As we will show, qualitative analyses are possible in this system but the combination of light and heavy elements presents serious challenges for quantitative analyses. These challenges include: difficulties in background fitting; dealing with effects of varying specimen thickness; obtaining sufficient signal to noise; separating contributions from overlapping edges with delayed maxima; finding high quality experimental standards; and the requirement to

normalise the signal to take into account elastic scattering effects. For qualitative analyses, we need methods of controlling the first four of these challenges. Quantitative analyses require us to deal with all of the challenges.

PZT thin films are of interest for use in applications such as non-volatile random access memory (RAM) devices. Ferroelectric thin films can be deposited by a number of methods including molecular beam epitaxy and pulsed laser deposition. The advantages of the sol-gel deposition method include the ability to deposit over large areas and the ease with which the composition or dopant level can be adjusted. However, structural and compositional inhomogenieties as well as interfacial phenomena can significantly influence the structure-property relationship. The film can either be deposited as one complete layer or in several stages. If the former method is used, cracking can occur during the firing stage (Impey et al., 1998); if the latter method is chosen, the resulting film can be seen to contain obvious layers from the different deposition stages (Impey et al., 1998; Huang et al., 1999). Previous work has shown variations in the elemental distributions across the deposition layers or film as a whole with the nature of these fluctuations depending upon the annealing conditions used (Impey et al., 1998; Sporn et al., 1995; Amanuma et al., 1994). Impey et al. (1998) used different analytical techniques to investigate variations in the elemental distributions within each sol-gel layer (resulting from the different deposition stages) and across the film as a whole. Results obtained by X-ray photoelectron spectroscopy (XPS), Auger electron spectroscopy (AES) and EDX analyses showed similar trends with fluctuations in the Zr and Ti signals at the interfaces between the sol-gel layers. However, the AES data also showed fluctuations in the Pb signal which were not apparent in either the XPS or EDX data. Here we investigate the ability of EELS to measure the elemental distributions.

2. Materials and Methods

2.1. Materials

A PZT film with nominal composition $Pb(Zr_{0.3}Ti_{0.7})O_3$ was supplied by Cranfield University and had been prepared by depositing PZT onto the Pt surface of a $Pt/Ti/SiO_2/Si$ (100) substrate by spin-coating a sol-gel solution. The deposition was performed in 10 stages with the film being annealed between the stages to induce crystallisation of the tetragonal perovskite structure (Zhang, 2004; Zhang and Whatmore, 2001). Cross-sectional TEM specimens of the film were prepared by standard grinding, polishing and dimpling methods. Final thinning was achieved by Ar ion milling in a Gatan precision ion polishing system (PIPS™).

Commercial powders of $PbTiO_3$, ZrO_2 and TiO_2 were used as experimental standards to provide reference edge shapes and Pb:O, Zr:O and Ti:O cross-section ratios. A commercial $PbZrO_3$ powder was also used to test the robustness of the quantification method. TEM specimens from these standards were prepared by crushing the powder in propanol in a pestle and mortar. Drops of the resulting suspensions were placed on holey carbon films on copper grids.

2.2. TEM

The specimens were examined in an FEI Tecnai F20 TEM/STEM (scanning transmission electron microscope) equipped with a field emission gun, a Gatan ENFINA™ electron spectrometer and an EDAX X-ray spectrometer. EELS, in the form of both spectroscopy and

spectrum imaging, was performed using Gatan DigiScan™ and Digital Micrograph™ software with the microscope operating in STEM mode.

Carbon contamination was found to be particularly problematic in the Pb-containing materials. In spite of the PZT cross-sections being plasma cleaned before being placed in the microscope, carbon did still build-up during data acquisition. Further difficulties were the formation of Pb droplets on the sample surface during the sample preparation and the sensitivity of the material to the electron beam.

To avoid damaging the PZT film, while still obtaining reasonable signal to noise, a probe current of ~0.02 nA was used along with a convergence semi-angle of 8.8 mrads and a collection semi-angle of 18 mrads. The edges chosen for analyses were the Pb $N_{6,7}$-edges, Zr $M_{4,5}$-edges, Ti $L_{2,3}$-edges and O K-edge. Using a dispersion of 0.5eV/channel, all of these edges could be collected in a single spectrum. The edge onsets are at ~138eV, ~180eV, ~455eV and ~532eV, respectively. It should be noted that the onset of the Pb $N_{6,7}$-edges have a very delayed maximum and the much weaker Pb O_1-edge has a threshold at 147. Therefore the Pb contribution present in the spectra is really a combination of the $N_{6,7}$-edges and the O_1-edge. For the PZT spectrum image (SI) data presented here, acquisition conditions of 1 read of 2 sec and 1 read of 2.5 sec per pixel were used corresponding to step sizes of 0.94 nm and 2.0 nm, respectively.

3. Results and discussion

Cross-sectional TEM analyses of the PZT film showed the presence of 10 layers in the film resulting from the 10 deposition stages. High resolution TEM examination of the sample showed no change of the crystallographic structure at the boundaries between the layers; the lattice fringes ran uninterrupted through the boundaries as shown in figure 1. As it is difficult to determine the physical extent of the boundary region in such an image, brackets on the figure indicate the approximate boundary position. However, as illustrated in figure 2, the boundaries showed up as narrow dark bands in high angle annular dark field (HAADF) STEM images. The intensity profile in figure 2(b) is the average profile from the box marked on figure 2(a) and reveals that the boundaries are a slightly brighter band followed by a darker band on moving from the substrate to the top surface. The decrease in overall intensity shows that the specimen becomes thinner towards the top surface. Although the resolution in the HRTEM image is greater than that in the STEM image, the boundaries show up more clearly in the STEM images as a result of the different mechanisms giving rise to the contrast in the respective images.

A typical EELS spectrum from PZT is shown in figure 3 with the background removed by fitting a power law of the form AE^{-r} in the region immediately prior to the onset of the Pb edges. The problem of the overlap of the Pb edges with the Zr $M_{4,5}$-edges is immediately obvious. The Pb signal can be mapped independently of the Zr signal using the Pb edge region prior to the onset of the Zr edge. But in order to quantify or map the Zr signal, it is necessary to isolate it from the underlying Pb signal. While it is possible to fit a power law background immediately prior to the Zr edge onset, this does not correctly isolate the Zr signal because of the delayed maximum in the Pb edge. However, the contributions from the Pb edge and the Zr edge can be successfully separated using a multiple linear least squares

(MLLS) fitting procedure to model the data as a linear combination of a Pb edge shape from $PbTiO_3$ and a Zr $M_{4,5}$-edge shape from ZrO_2. Note that, while no weighting scheme was utilised in the MLLS fitting used here, as discussed below the Zr fit is more susceptible to error. For early work on multiple least squares fitting of EELS spectra see Shuman and Somlyo, 1987 and Leapman and Swyt, 1988.

For mapping and quantification purposes, the use of different energy windows was investigated. For the results presented here, an energy window of 145-240eV was used for the Pb signal in $PbTiO_3$ and the combined Pb+Zr signal in $PbZrO_3$ and PZT. A window of 180-240eV was used for the Zr signal in ZrO_2. 70eV and 30eV wide windows starting at the edge onsets were used for the Ti and O edges, respectively, in all samples. The width of the O window was limited to 30eV in order to avoid incorporating signal from the Ti L_1-edge, which has an onset at 564eV. Varying the width of the combined Pb+Zr window to cover the energy ranges 145-240eV; 140-240eV and 145-280eV, was found to make differences of ~3% to the final atomic ratios obtained. For the data presented here, 145-240eV is used. For quantitative analyses the reference spectra were scaled appropriately using their O K-edges. The MLLS fit was performed over the energy range 145-240eV using background subtracted edges. For comparison, the Pb signal was also mapped directly using the energy range 145-180eV.

Lower lying metal edges make the Pb+Zr background-subtracted signal very sensitive to the window used for background subtraction. Using the window 130-141eV was found to give the most consistent results. This may indicate a chemical shift of the Pb $N_{6,7}$-edges or just be a result of the very delayed maximum of this edge. A further difficulty is with the

background subtraction of the O edge in the presence of Ti. One is initially tempted to fit a narrow window in the 509-526eV range but this is very sensitive to the Ti fine structure, in particular to the broad bump in the ~500-520 eV range, and can lead to an overestimate of the O signal in Ti-containing samples where the bump is very distinct. It was found that using a window running from 466-526eV gave the most consistent results in terms of simple power law background subtractions. While the use of such a power law background subtraction is clearly not ideal it did actually provide a simple and workable method of isolating the O signal in this case.

In order to test the robustness of the MLLS fitting method, the same approach was adopted to separate the edges in data from the $PbZrO_3$ standard. Figure 4(a) shows the reference edges from the $PbTiO_3$ and ZrO_2 while the edges from $PbZrO_3$ are shown in figures 4(b) and 4(c) along with the result of the MLLS fit. Table 1 lists all of the background and integration windows used in this analysis. The Pb:O and Zr:O ratios were determined by integrating the counts in the relevant windows and using the experimentally determined cross-section ratios. The Pb:O ratio was also determined using the non-MLLS route. In $PbTiO_3$ the Ti:O ratio was also quantified using the TiO_2 as the reference standard. The atomic fraction values obtained are listed in table 2 and are within 1%, 5% and 11% of the expected values for the Ti/O, Pb/O and Zr/O, respectively. Such agreement is excellent bearing in mind the elements under consideration and the MLLS methodology required to extract the Zr signal from the Pb signal. One of the reasons why the Pb/O value obtained from the MLLS fitting is more accurate than the Zr/O, is the ~35eV window prior to the Zr onset in which the routine fits to the isolated Pb signal. This ~35eV window has two effects: firstly it means that the Pb signal is being fitted over a larger energy window; secondly it will force the Pb fit in this region and

hence the whole window. This means that the Zr fit is likely to be more sensitive to noise in the spectra and hence more susceptible to error. The situation is worse in PZT where there is relatively less Zr present.

The experimentally determined partial cross-section ratios are listed in table 3. Also given are the values calculated using the Hartree-Slater theoretical cross-sections in Digital Micrograph™; theoretical cross-sections were unavailable for the Pb N-edges. One can see that while the theoretical partial cross-section ratio for O/Ti is within ~2% of the experimental value, that of O/Zr is out by more than 40%. Thus, as noted previously by Hofer and Kothleitner (1996), the use of experimental standards in compositional analysis of materials containing heavier elements is essential.

In order to investigate the uniformity of the PZT film composition and, in particular, any changes in composition associated with the boundaries, EELS spectrum images were acquired. Figures 5(a) and 6(a) show HAADF STEM images of the PZT film with the spectrum image regions indicated by black boxes; the white boxes show the regions used for spatial drift correction during acquisition. Note that the growth direction is right to left in these datasets. Two examples are given: the first shows the variation across a boundary between two of the sol-gel layers in a thin region ($t/\lambda \leq 0.35$) of the TEM sample; the second shows the variation across a complete sol-gel layer but extends into a thicker region of the sample with a variation in t/λ from 0.25 to 0.45. The spectrum images were processed as follows. Energy drift in the spectrum image was corrected to first order by aligning the Ti white lines. Maps were created of the Ti, O, Pb and combined Pb+Zr signals by removing appropriate backgrounds and integrating the intensity in the relevant windows. A

background subtracted spectrum image with the background subtracted under the Pb edges was created. The spectra in this background subtracted SI were then MLLS fitted using the scaled Pb and Zr reference edges. An example of such a fit is given in figure 4(d); the data corresponds to the first pixel in the spectrum image corresponding to figure 5. One can immediately see that the Zr edge is difficult to discern on the back of the Pb edge and that the Zr fit will be more sensitive to the noise in the spectrum image than the Pb fit. The relative weightings from the fit were used to create Pb and Zr maps. Figures 5(b) and 6(b) show the Pb and Zr maps obtained this way as well as the maps for Ti, O, Pb and Pb+Zr produced by simple power law background subtraction and integration. The Zr and Ti maps clearly show intensity variations associated with the boundary positions.

Ti/O, Pb/O and Zr/O count maps were obtained by dividing the Ti, Pb and Zr maps by the O map. These were converted to Ti/O, Pb/O and Zr/O atomic maps by scaling with the appropriate experimental cross-section ratios. (Ti+Zr)/O and (Pb+Ti+Zr)/O atomic maps were created by summing the individual metal/O atomic maps. Line profiles obtained from these metal/O atomic maps are shown in figures 5(c) and 6(c). Pixels parallel to the interfaces were averaged in these maps using all of the rows in the data in figure 5 and the top 10 rows in figure 6, as the lower half appeared to have suffered some beam damage from earlier exposure.

While the (Ti+Zr):O ratio is uniform in both spectrum images, the complementary nature of the Ti:O and Zr:O ratios can be clearly seen. The Ti concentration decreases in the growth direction in each sol-gel layer while the Zr increases. This results in a Zr rich and Ti depleted region immediately followed by a Ti rich and Zr depleted region at the boundaries between

the layers. This explains the bright and dark bands apparent in the HAADF STEM images of the boundaries with the Zr rich region being bright and the Ti rich region being dark. The Pb:O ratio is essentially uniform in the thinner regions of the SIs but can be seen to decrease when moving into the thicker region of the second SI (figure 6). The t/λ varied from ~0.25 to 0.45 over the range of this spectrum image.

The fluctuations observed in the elemental profiles may be understood as follows. In the perovskite structure the Pb atoms occupy the A^{2+} site while the Ti and Zr atoms substitute on the B^{4+} site. Thus one might expect that the Pb:O and (Ti+Zr):O ratios would be constant but that the Ti:Zr ratio could fluctuate as a result of substitution on the B^{4+} site. $PbTiO_3$ crystallises at a lower temperature than $PbZrO_3$ and hence, as each layer crystallises, it is initially Ti rich and gets gradually Zr enriched (note the slow rise of Zr/O across the layer) and ends as Zr-rich when the remaining Zr enriched material finally crystallises (Sporn et al., 1995).

The average composition of the sol-gel layer was estimated as follows. The mid-boundary to mid-boundary distance in figure 6(c) was determined as 74.6nm and the mean of the values between 0 and 74.6nm, i.e. the thinner region, in figure 6(c) was taken. The results are given in table 4 along with the nominal composition. The quantification gives Ti/O and Pb/O values which are within ~1% and ~10% of the expected values, respectively. However, the Zr/O value, which is more susceptible to error in the fitting, is out by almost a factor of 2. Possible reasons for this discrepancy are (i) an effect of electron beam damage although this seems unlikely, as one would not expect to preferentially lose Zr in this manner; (ii) a systematic error arising from the processing; (iii) the reference data spectra used in the MLLS

fits of the PZT spectrum image data are from regions of material of significantly different thickness.

Clearly there are problems with the background removal under the Pb edge in the case of thicker materials and it is better to work with thinner sections. However, thinner sections are more sensitive to beam damage and the presence of the Pb droplets on the surface. Data sets collected from thinner regions with shorter acquisition times showed higher and more uniform levels of Pb. One way to improve the data would be to acquire new datasets using sub-pixel scanning which is now available and in which the probe is scanned over the whole area of the pixel during acquisition rather than being held at a single point within the pixel. In data sets such as the ones presented here, where the probe size is considerably smaller than the pixel size, sub-pixel scanning would spread the electron dose uniformly over the pixel and hence reduce the beam damage. A second method to facilitate improvements would be to acquire the low loss spectra under the same optical conditions. For the collection conditions used here, it was not possible to reduce the acquisition time sufficiently to allow acquisition of an unsaturated zero loss peak, as the electromagnetic shutter in the spectrometer sets a limit on the shortest integration times available. Since the acquisition of the PZT data reported here, the Glasgow Tecnai F20 has been fitted with a fast beam switch in one of the camera ports above the viewing screen. The fast beam switch permits rapid shuttering of the beam and hence greater flexibility in controlling the intensity entering the Enfina CCD (Craven, Wilson and Nicholson, 2002). This has been integrated into the spectrum image acquisition system so that high quality core edge and low loss spectra can now be acquired at each pixel using the same electron optical conditions (Scott et al., 2007). Use of this fast beam switch to acquire low loss spectra under the same conditions would provide a much better knowledge of

the background in front of the Pb edges and allow further processing of the data such as Fourier-log deconvolution (Egerton, 1996). This would make the background subtraction and the use of standards in MLLS fitting much more robust leading to improved extraction of the Zr contribution. It should be noted that low loss spectrum images could be successfully acquired from the PZT sample albeit with different acquisition conditions, e.g., a different collection angle and different energy dispersion. However, because of these differences in acquisition conditions, it is necessary to acquire such datasets sequentially i.e. one complete spectrum image followed by another, and it is then difficult to ensure perfect spatial registration of pixels between the different datasets. Here we have not attempted removal of plural scattering via low loss spectra acquired under different electron optical conditions.

Another possible method of improving the Zr quantification would be to extend the MLLS fitting region to include the Zr $M_{2,3}$-edges. In order for this to work it would be necessary to either acquire C-free spectra or include an amorphous C K-edge in the MLLS fitting. Applying more advanced methods of background subtraction, such as scaling and subtracting a Ti edge shape, obtained from unoxidised Ti or TiN, would also allow the use of a larger O window. In principle MLLS fitting of the Ti and O edges could also be used to isolate the signals. However, to do this successfully one would require O and Ti edges from suitable standards in which the fine structure provided reasonable matches to that of the PZT, TiO_2 and $PbTiO_3$ used here. Finding such edges is non-trivial. Initial attempts at MLLS fitting using a Ti edge from TiC and an O edge from SiO_2 did not actually improve the analysis but will be investigated further.

Nonetheless, the ability to extract results such as those demonstrated here, from a system containing both Pb and Zr and in which there is a large degree of edge overlap, is an excellent achievement. In future it is hoped to improve the reliability of the MLLS fitting and also to extend these techniques to other systems of interest containing heavy elements.

4. Conclusions

In summary, the changes in chemistry at the boundaries between deposition layers in a PZT film are observed in HAADF STEM images. A MLLS fitting routine was used to successfully separate the overlapping Pb and Zr signals with the result that excellent qualitative analyses of the four elements present in the system was achieved. EELS spectrum imaging has shown that the boundaries are Ti rich at the start of a new layer and Zr rich at the end with the Pb/O and (Ti+Zr)/O remaining constant, as expected from the continuous lattice fringes across the boundaries. Quantitative analysis gave good results for Ti/O and Pb/O but the Zr/O results are less satisfactory, indicating that the separation of Zr from Pb remains problematic. Further refinement in both acquisition and processing are required and there are good routes available for this.

Acknowledgements

The authors would like to thank Dr S. McFadzean and Mr B. Miller (University of Glasgow) for technical support and the EPSRC for funding PH. Dr Z. Huang (Cranfield University) is thanked for providing the PZT film.

References

Amanuma, K., Hase, T. and Miyasaka, Y., 1994. Crystallization behavior of sol-gel derived $Pb(Zr,Ti)O_3$ thin films and the polarization switching effect on film microstructure. Applied Physics Letters 65, 3140-3142.

Craven, A.J., Wilson, J.A. and Nicholson, W.A.P., 2002. A fast beam switch for controlling the intensity in electron energy loss spectrometry. Ultramicroscopy 92, 165-180.

Egerton, R.F., 1996. Electron Energy Loss Spectroscopy in the Electron Microscope, 2nd Ed, Plenum, New York.

Impey, S.A., Huang, Z., Patel, A., Beanland, R., Shorrocks, N.M., Watton, R. and Whatmore, R.W., 1998. Microstructural characterization of sol-gel lead-zirconate-titanate thin films. Journal of Applied Physics 83, 2202-2208.

Hofer, F. and Kothleitner, G., 1996. Quantitative microanalysis using electron energy-loss spectrometry: II. Compounds with heavier elements. Microscopy Microanalysis Microstuctures 7, 265-277.

Huang, Z., Zhang, Q. and Whatmore, R.W., 1999. Low temperature crystallization of lead zirconate titanate thin films by a sol-gel method. Journal of Applied Physics 85, 7355-7361

Leapman, R.D. and Swyt, C.R., 1988. Separation of overlapping core edges in electron energy loss spectra by multiple-least-squares fitting. Ultramicroscopy 26, 393-404.

Scott, J., Craven, A.J., Thomas, P.J., MacKenzie, M., McFadzean, S., Wilbrink, J., and Nicholson, W.A.P., 2007. Multiple energy range EELS. To be submitted to Ultramicroscopy

Shuman, H. and Somlyo, A.P., 1987. Electron energy loss analysis of near-trace-element concentrations of calcium. Ultramicroscopy 21, 23-32.

Sporn, D., Merklein, S., Grond, W., Seifert, S., Wahl, S. and Berger, A., 1995. Sol-gel processing of perovskite thin films. Microelectronic Engineering 29, 161-168.

Zhang, Q. and Whatmore, R.W., 2001. Sol-gel PZT and Mn-doped PZT thin films for pyroelectric applications. Journal of Physics D: Applied Physics 34, 2296-2301

Zhang, Q., 2004. Effects of Mn doping on the ferroelectric properties of PZT thin films. Journal of Physics D: Applied Physics 37, 98-101

Figure captions

Figure 1 High resolution TEM image of an interface between two sol-gel layers showing lattice fringes continuing over the boundary; the approximate extent of the boundary is indicated by the brackets at the top and bottom of the figure.

Figure 2 (a) HAADF STEM image of the PZT film showing the 10 sol-gel layers and the underlying Pt, Ti and SiO_2. (b) Variation in intensity across the upper sol-gel layers averaged over the region marked by the box in (a). Arrows indicate the boundary positions. Note that the intensity scale has been offset and expanded to highlight the variation at the boundaries.

Figure 3 Typical EELS spectrum from PZT showing the Pb, Zr, O and Ti edges. The C K-edge is also indicated.

Figure 4 (a) EELS spectra from $PbTiO_3$ and ZrO_2 showing the overlap of the Pb and Zr edges. (b) EELS spectrum from $PbZrO_3$ and the result of an MLLS fit using $PbTiO_3$ and ZrO_2 reference spectra. (c) As for (b) but expanded to show the fit more clearly. (d) EELS spectrum from the first pixel in the spectrum image relating to figure 5 below and the result of the MLLS fit using $PbTiO_3$ and ZrO_2 reference spectra.

Figure 5 (a) HAADF STEM image of the PZT film showing the region, marked with a black box, from which an EELS spectrum image was acquired; the white box indicates the region used for drift correction. (b) Maps of the Ti, O, Pb, Pb+Zr, MLLS Pb and MLLS Zr signals obtained from the spectrum image. (c) Graphs of atomic fraction ratios obtained using the maps in (b) along with the relevant cross-section ratios.

Figure 6 (a) HAADF STEM image of PZT film showing the region, marked with a black box, from which an EELS spectrum image was acquired; the white box indicates the

region used for drift correction. (b) Maps of the Ti, O, Pb, Pb+Zr, MLLS Pb and MLLS Zr signals obtained from the spectrum image. (c) Graphs of atomic fraction ratios obtained using the first 10 rows in the maps in (b) along with the relevant cross-section ratios.

Table 1. Background and integration windows used for $PbTiO_3$, ZrO_2, $PbZrO_3$ and PZT analyses.

Edge	Background window (eV)	Integration window (eV)
Pb $N_{6,7}$	130-141	145-180
Pb $N_{6,7}$ + Zr $M_{4,5}$	130-141	145-240
MLLS Pb $N_{6,7}$	130-141	145-240
Zr $M_{4,5}$	146-175	180-240
Ti $L_{2,3}$	370-440	455-525
O K	466-526	528-558

Table 2. Nominal and experimentally determined atomic fractions obtained from $PbZrO_3$ and $PbTiO_3$ using reference standards.

Sample	Atomic fraction	Reference standard	MLLS	Nominal	Measured
$PbZrO_3$	Pb/O	$PbTiO_3$		0.333	0.33
$PbZrO_3$	Pb/O	$PbTiO_3$	yes	0.333	0.35
$PbZrO_3$	Zr/O	ZrO_2	yes	0.333	0.37
$PbTiO_3$	Ti/O	TiO_2		0.333	0.33

Table 3. Comparison between our experimental partial cross-section ratios and those obtained using the Hartree-Slater cross-sections within Digital Micrograph™.

Reference standard	Ratio	Experimental partial cross-section ratio	Hartree-Slater partial cross-section ratio	Pb window
$PbTiO_3$	O/Pb	0.147	N/A	145-180
$PbTiO_3$	O/Pb	0.0396	N/A	145-240
ZrO_2	O/Zr	0.0424	0.0238	
TiO_2	O/Ti	0.0851	0.0867	

Table 4. Nominal and the average experimentally determined atomic fractions over one complete PZT layer. The standard deviation on the measured mean is also given.

Atomic fraction	Reference standard	MLLS	Nominal	Measured mean	Standard deviation
Ti/O	TiO_2		0.223	0.22	0.024
Pb/O	$PbTiO_3$		0.333	0.30	0.029
Pb/O	$PbTiO_3$	yes	0.333	0.30	0.034
Zr/O	ZrO_2	yes	0.100	0.054	0.021
(Ti+Zr)/O	-		0.333	0.28	
(Pb+Ti+Zr)/O	-		0.667	0.58	

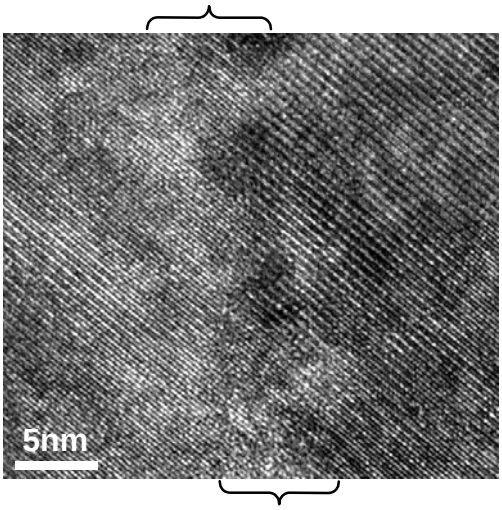

FIGURE 1

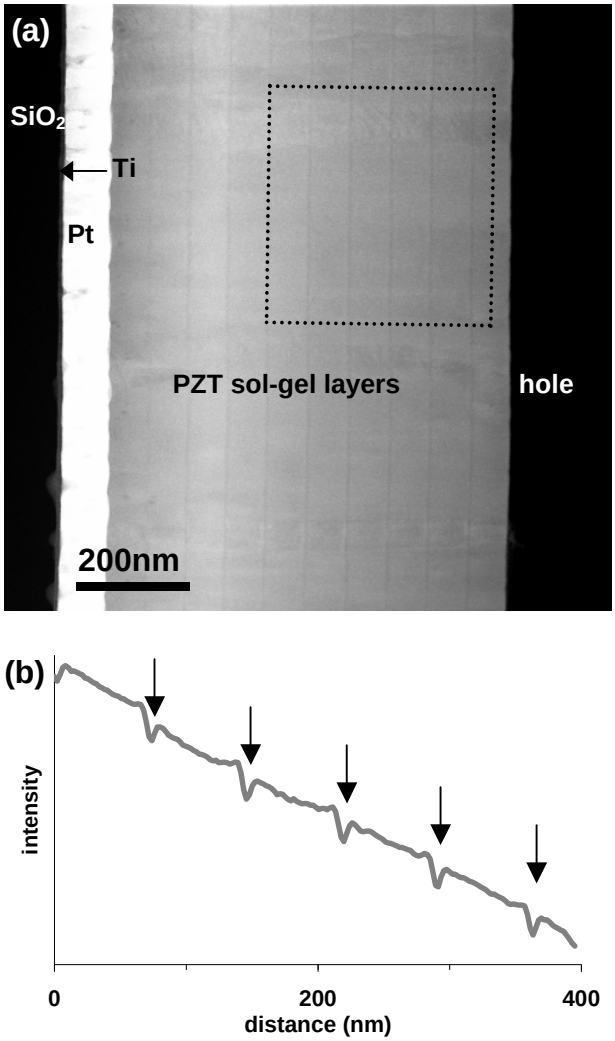
(a)
SiO2
Ti
Pt
PZT sol-gel layers
hole
200nm
(b)
intensity
0
200
400
distance (nm)

FIGURE 2

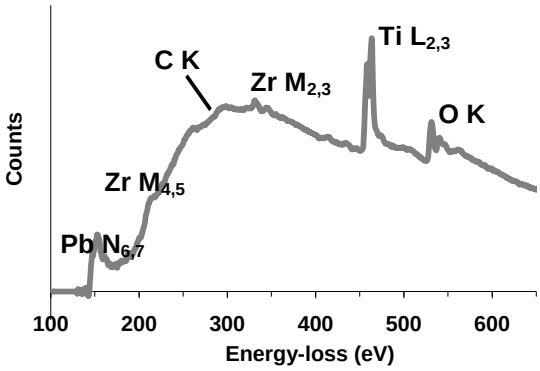
Ti L2,3
C K
Zr M2,3
O K
Zr M4,5
Pb N6,7
Counts
100
200
300
400
500
600
Energy-loss (eV)

FIGURE 3

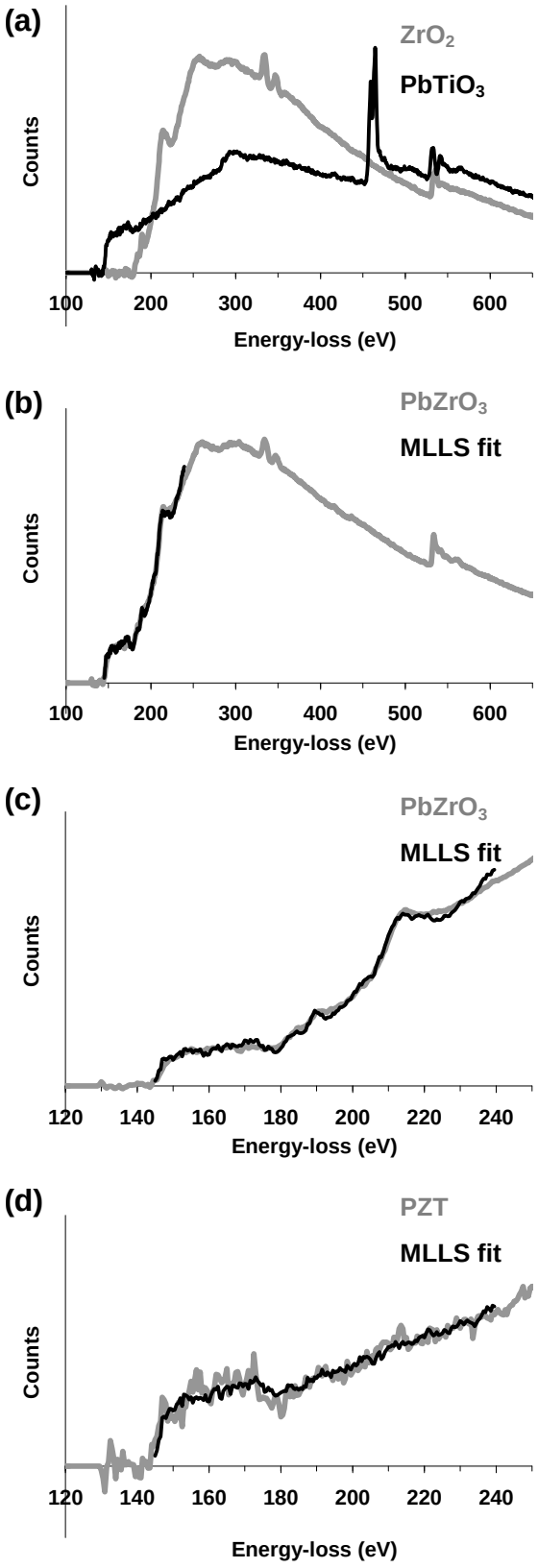
(a)
ZrO2
PbTiO3
Counts
100
200
300
400
500
600
Energy-loss (eV)
(b)
PbZrO3
MLLS fit
Counts
100
200
300
400
500
600
Energy-loss (eV)
(c)
PbZrO3
MLLS fit
Counts
120
140
160
180
200
220
240
Energy-loss (eV)
(d)
PZT
MLLS fit
Counts
120
140
160
180
200
220
240
Energy-loss (eV)

FIGURE 4

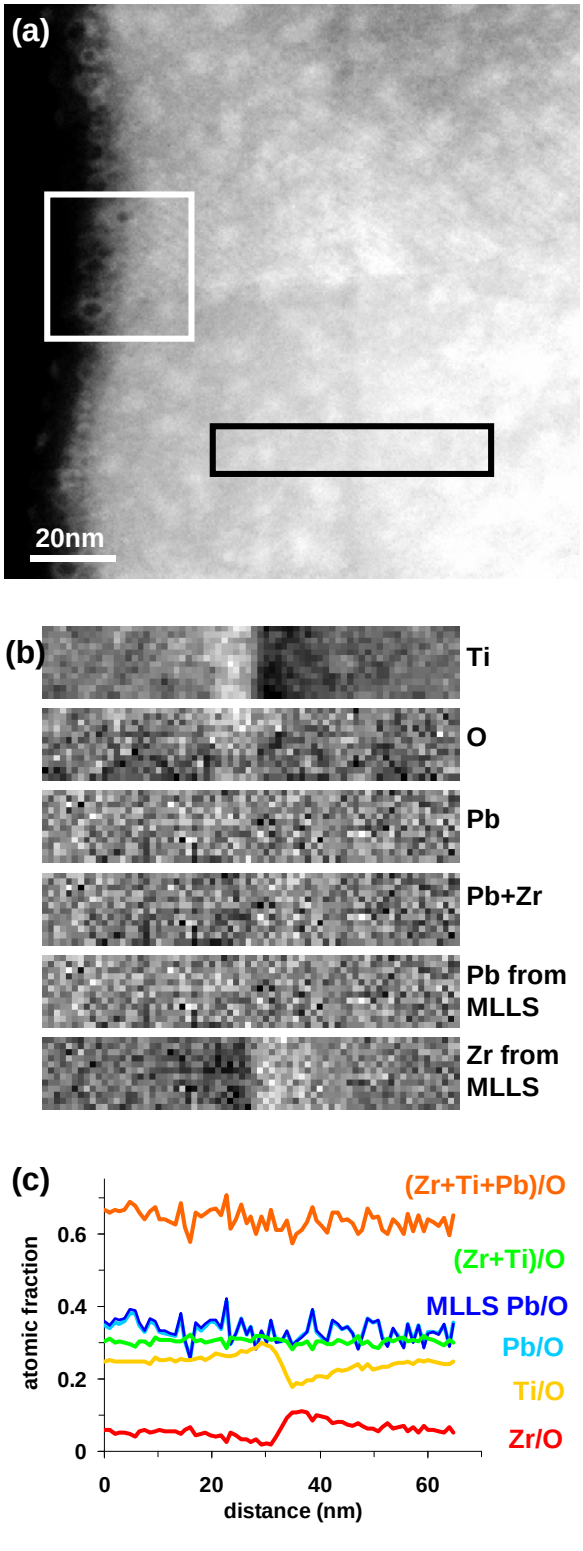
(a)
20nm
(b)
Ti
O
Pb
Pb+Zr
Pb from MLLS
Zr from MLLS
(c)
(Zr+Ti+Pb)/O
(Zr+Ti)/O
MLLS Pb/O
Pb/O
Ti/O
Zr/O
atomic fraction
0
0.2
0.4
0.6
0
20
40
60
distance (nm)

FIGURE 5

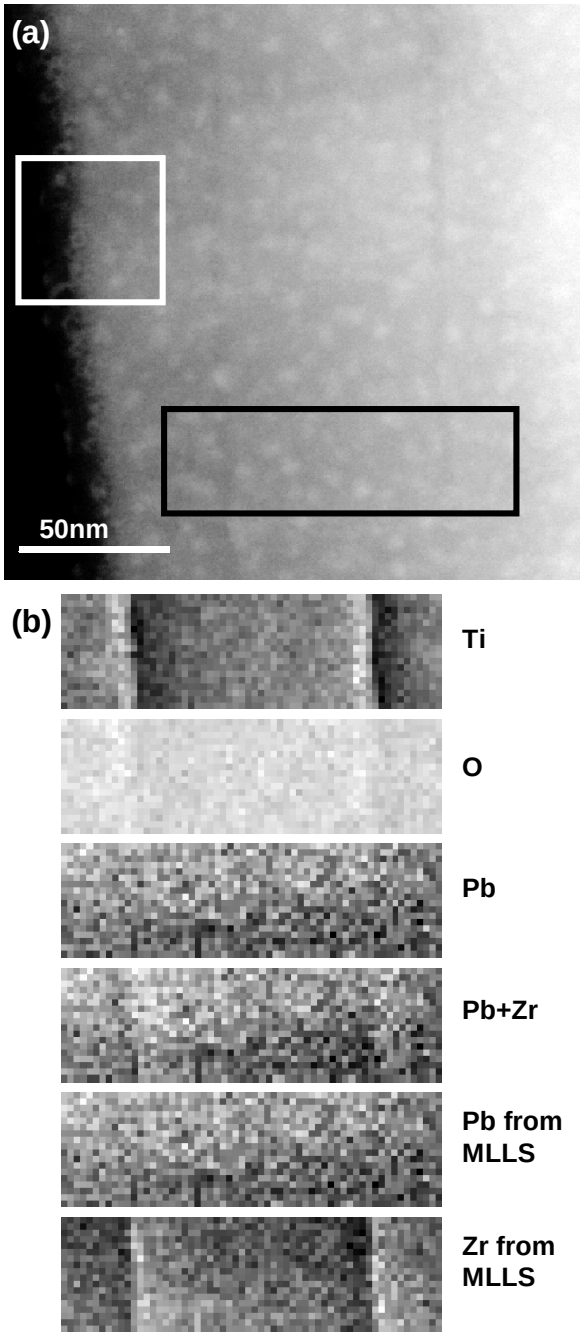
(a)
50nm
(b)
Ti
O
Pb
Pb+Zr
Pb from MLLS
Zr from MLLS
(c)
(Zr+Ti+Pb)/O
(Zr+Ti)/O
MLLS Pb/O
Pb/O
Ti/O
Zr/O
atomic fraction
0
0.2
0.4
0.6
0
20
40
60
80
100
120
distance (nm)

FIGURE 6